

 Open access • Journal Article • DOI:10.1021/ACSNANO.9B09685

Two-Step Patterning of Scalable All-Inorganic Halide Perovskite Arrays.

— [Source link](#) 

Chung-Kuan Lin, Chung-Kuan Lin, Qiuchen Zhao, Ye Zhang ...+6 more authors





Institutions: Lawrence Berkeley National Laboratory, University of California, Berkeley

Published on: 20 Feb 2020 - ACS Nano (ACS Nano)

Topics: Perovskite (structure) and Halide

Related papers:

- [Monocrystalline halide perovskite nanostructures for optoelectronic applications](#)
- [Progress in organic-inorganic hybrid halide perovskite single crystal: growth techniques and applications](#)
- [Single-Crystal Thin Films of Cesium Lead Bromide Perovskite Epitaxially Grown on Metal Oxide Perovskite \(SrTiO₃\)](#)
- [A general printing approach for scalable growth of perovskite single-crystal films](#)
- [Tunable cathodoluminescence over the entire visible window from all-inorganic perovskite CsPbX₃ 1D architecture](#)

Share this paper:    

View more about this paper here: <https://typeset.io/papers/two-step-patterning-of-scalable-all-inorganic-halide-4ddj7zhubx>

UC Berkeley

UC Berkeley Previously Published Works

Title

Two-Step Patterning of Scalable All-Inorganic Halide Perovskite Arrays.

Permalink

<https://escholarship.org/uc/item/7n39206q>

Journal

ACS nano, 14(3)

ISSN

1936-0851

Authors

Lin, Chung-Kuan
Zhao, Qiuchen
Zhang, Ye
et al.

Publication Date

2020-03-01

DOI

10.1021/acsnano.9b09685

Peer reviewed

Two-step patterning of scalable all-inorganic halide perovskite arrays

*Chung-Kuan Lin^{1, 2+}, Qiuchen Zhao¹⁺, Ye Zhang^{1, 2}, Stefano Cestellos-Blanco³, Qiao Kong¹, Minliang Lai¹, Joohoon Kang,^{1, 4, 5, 6} Peidong Yang^{1, 2, 3, 4, *}*

¹ Department of Chemistry, University of California Berkeley, Berkeley, California 94720, USA.

² Materials Sciences Division, Lawrence Berkeley National Laboratory, Berkeley, California 94720, USA.

³ Department of Materials Science and Engineering, University of California Berkeley, Berkeley, California 94720, USA.

⁴ Kavli Energy NanoScience Institute, Berkeley, California 94720, USA.

⁵ Center for NanoMedicine, Institute for Basic Science (IBS); Y-IBS Institute, Yonsei University, Seoul, Korea

⁶ School of Advanced Materials Science and Engineering, Sungkyunkwan University (SKKU), Suwon, Korea

+ These authors contributed equally to this work.

*Correspondence should be addressed to P.Y. (p_yang@berkeley.edu)

KEYWORDS: halide perovskite, patterned growth, chemical vapor transport

ABSTRACT

Halide perovskites have many important optoelectronic properties, including high emission efficiency, high absorption coefficients, color purity and tunable emission wavelength, which makes this material promising for optoelectronic applications. However, the inability to precisely control large-scale patterned growth of halide perovskites limits their potential toward various device applications. Here, we report a patterning method for the growth of cesium lead halide perovskite single crystal array. Our approach consisted of two steps: (1) cesium halide salt arrays patterning and (2) chemical vapor transport (CVT) process to convert salt arrays into single crystal perovskite arrays. Characterizations including energy-dispersive x-ray spectroscopy and photoluminescence have been employed to confirm the chemical compositions and the optical properties of the as-synthesized perovskite arrays. This patterning method enables the patterning of single crystal cesium lead halide perovskite arrays with tunable spacing (from 2 μm to 20 μm) and crystal size (from 200 nm to 1.2 μm) in high production yield (almost every pixel in the array is successfully grown with a converted perovskite crystals). Our large-scale patterning method renders a platform for study of fundamental properties and opportunities for novel perovskite-based optoelectronic applications.

Introduction

Lead halide perovskites, corner-shared octahedral structures with typical formula of APbX_3 ($\text{A} = \text{Cs}^+$, CH_3NH_3^+ , $\text{X}=\text{Cl}^-$, Br^- , I^-), have excited the community with many important optoelectronic properties, such as high emission efficiency¹, high absorption coefficients², color purity and tunable emission wavelength³. These properties have made perovskite a strong candidate for optoelectronic applications, such as light emitting diodes (LEDs)⁴, photodetectors⁵⁻⁸ and lasers^{9, 10}. The ability to create periodic array structure is of central importance to develop various optoelectronic applications. However, its chemical instability in various solvents and ambient conditions^{11, 12} makes current nanofabrication techniques difficult to be applied directly to perovskites.

To date, diverse efforts have been developed to produce perovskite arrays, including direct and indirect patterning methods¹³. The main advantage of direct patterning is that it allows for high-spatial resolution. A typical method for direct patterning is ink-jet printing^{14, 15}, which creates spatially controlled polycrystalline¹⁶⁻¹⁸ or single crystal perovskite arrays^{14, 19} with careful optimization of precursor amounts. Another direct patterning approach consists of employing a focused ion beam (FIB)²⁰ or laser beam²¹ to etch and transform perovskite thin films into intended patterns^{20, 22}. Other common approaches for direct patterning are micro/nano-imprint methods²³, which utilize molds (typically made by PDMS) with designed patterns. Perovskite

precursors (usually gel²⁴ or solution²⁵) are firstly deposited on a substrate, and the mold is placed with a certain pressure on the top. The periodic pattern underneath is created after evaporation of solvents. These direct patterning methods can reach micro-scale precision, and can be achieved by programmable arbitrary patterns with ink-jet printing.

Indirect patterning, on the other hand, provides process scalability. In this method, various pre-treatments are employed to obtain patterns on substrates, followed by selective growth of periodic perovskite structures²⁶⁻²⁸. Periodic two-dimensional (2D) material arrays such as graphene^{26, 27} or boron nitride²⁶, or hydrophilic/hydrophobic patterns by surface modification methods are widely used to grow perovskite crystal arrays²⁸. In 2015, Duan and co-workers designed a method, using octadecyltrichlorosilane (OTS) monolayer pattern on a Si/SiO₂ substrate, to define hydrophilic areas on a hydrophobic surface, followed by a seed growth to create Pbl₂ arrays²⁸. The Pbl₂ arrays were converted into (CH₃NH₃)Pbl₃ by a gas-solid process with methylammonium iodide vapor. This bottom-up method not only preserved the crystallinity of perovskites but also paved the way for large scale patterned growth.

However, hybrid perovskite optoelectronics are still facing the challenges of stability under ambient conditions^{11, 12} and their all-inorganic counterpart could therefore be a candidate to overcome these difficulties due to their

better thermal, oxygen and moisture stability²⁹⁻³¹. Simply adopting the patterning method from hybrid halide perovskite case to the all-inorganic version may not be applicable due to the lower vapor pressure of inorganic halide compared with the methylammonium halide. Here we report a two-step patterning method to produce single crystal all-inorganic perovskite arrays. This method exploits the melting temperature difference between CsX and PbX₂ (X=Cl⁻, Br⁻, I⁻) and soft ionic bonding nature of perovskite structure. Cesium halide (higher melting point) arrays were grown on a pre-patterned hydrophobic/hydrophilic surface and then a chemical vapor transport (CVT) process is used to convert the CsX into CsPbX₃ perovskite arrays. This method can be generalized and extended to all three halides (Cl⁻, Br⁻, I⁻) that are typically used for emission color tunability of the halide perovskite family. A series of characterization methods were carried out to further confirm the composition of the as-grown perovskite arrays. Our method allows us to grow scalable single crystal inorganic halide perovskite arrays with controllable crystal size (from 200 nm to 1 μm) and spacing (from 2 μm to 20 μm) in high production yield (every pixel in the array is successfully grown with a converted perovskite crystals). Furthermore, this approach renders a platform to develop novel perovskite optoelectronics, such as high-quality LED displays and high-sensitive photodetectors. Moreover, our scheme has enabled the patterned growth of perovskite arrays on wafer-scale Si substrate, creating a pathway for integrating perovskite emitters with Si photonics.

Results and Discussion

Perovskite crystal arrays were successfully grown in a two-step patterning process that involved a pre-patterned substrate, growth of CsX arrays, and conversion to perovskite crystals (Figure 1a). A patterned substrate with wettability contrast was designed by photolithography and a subsequent surface modification process (more details are shown in SI method). Cesium halide aqueous solution was flowed through the patterned substrate (Figure 1a, step 2), and droplets of the CsX solution were confined in hydrophilic squares. The CsX preferentially nucleated inside the square area (Figure 1a, step 3) after evaporation of the solvent. These CsX were each converted into CsPbX₃ perovskite crystals through a chemical vapor transport (CVT) conversion process (figure 1b), by using a PbX₂ solid precursor with the same halide. Figure 1c shows the SEM image before (left, CsX salt) and after (right, perovskite crystal) conversion in an individual window. This demonstrated that the polycrystalline salt can be converted into a cubic-shaped perovskite, and in most of the windows a single nucleus formed.

Variations in surface modifications in the patterning process resulted in differing perovskite crystal features. A typical hydrophobic surface modification agent²⁸, OTS (CH₃(CH₂)₁₇SiCl₃), was employed in our patterning process to form a hydrophobic self-assembled monolayers (SAMs) grid. OTS reacted with hydroxyl groups on the SiO₂ surface, a Si-O bond formed and the surface was modified with long chain alkyl groups (C₁₈H₃₇·, shown in

Figure 2a, top row middle case). The wettability contrast between hydrophilic square area (SiO_2) and hydrophobic grid (OTS) would confine solution droplets when CsX aqueous solution flowed through. During the dewetting process, patterned substrate with suitable wettability conditions plays an important role in obtaining CsX arrays^{14, 32-35}. We hypothesized that the dewetting dynamics, including droplet confinement, evaporation, and evolution of the three-phase contact line would depend on the wettability between surface and droplets³⁵. This process was essentially a competition between pinning forces (because of solvent and substrate surface interaction) and depinning forces (deviation of the droplet profile from equilibrium due to evaporation). During evaporation of the solvent, the contact line was anchored on wetting substrate³⁶ (Figure 2b, top row), but receded on non-wetting substrates³⁷ (Figure 2b, bottom row). As the solvent evaporated, and when the concentration of the solution reached a supersaturated critical point, CsX precipitated and nucleated on the surface. For the wetting substrate (as shown in Figure 2b top row), the nucleation took place over the whole square due to anchored contact line, and resulted in multiple nucleation sites. On the contrary, when the substrate was non-wetting, the contact line of the droplet on the surface (see Figure 2b bottom row) receded significantly at the critical concentration, and the salt precipitated in a localized area.

To further control wettability of the inner-square area, we employed methyltrichlorosilane (MTS) as a surface modification agent, and systematically studied the relationship between surface wettability and CsX nucleation. The SiO₂ surface was first treated with NaOH, then immersed in dilute MTS-hexane solution (1:25000) for various amounts of time (4 mins, 6 mins, and 60 mins). This procedure allowed us to control wettability contrast in the inner square area. The original OTS grid was not affected by NaOH or MTS treatment (shown in Figure S1). NaOH activated the bare SiO₂ surface with hydroxyl groups to make it hydrophilic due to hydrogen bonding interaction between substrate and solvent. When MTS reacted with the NaOH-modified substrate, the Si-O bond formed and the surface was functionalized by methyl groups. MTS has a shorter alkyl chain (Figure 2a) compared to OTS. The surface with methyl groups was more hydrophobic than the surface with hydroxyl groups, but was less hydrophobic compared with OTS-modified surface.

The MTS coverage increased with the immersion time as indicated by the contact angle measurement (Figure 2c), used to quantify the interaction between substrate and droplets. Varying the immersion time from 0 to 10 minutes resulted in the change of contact angle from 30° to 86°, demonstrating that the wettability of the inner-square area can be effectively controlled. With a short immersion time, inner-square area was sparsely covered by MTS (Figure 2a bottom row, middle case), and the contact angle

is relatively small, indicating a stronger droplet-substrate interaction. On the contrary, with longer immersion time, the surface was densely covered by MTS (as shown in Figure 2a bottom row, right hand-side case), and the surface would be more hydrophobic and resulted in weaker interaction with the droplet. However, after a 60 min immersion time in MTS, the contact angle remained almost constant.

The SEM was used to further examine the morphology of CsX nucleation sites under various wettability conditions. The SEM images of the as-patterned crystal morphology shown in figure 2d correspond to the substrate immersed in MTS for 0 min (NaOH treatment only), 4 min, 6 min, and 60 min, respectively, and CsCl was selected as a representative for discussion. In the case of high wettability, with fully wetting substrate (NaOH treatment only, no MTS treatment, with the contact angle around 30°), the CsX tended to form multiple nucleation sites. With moderate wettability, partially wetting substrate (immersed in MTS solution from 4 to 6 mins, with the contact angle around 65° and 75° respectively), the CsCl with polycrystalline morphology, localized distribution and dendritic structure was obtained. When the substrate was too non-wetting (after 60 min MTS treatment, with the contact angle around 86°), no salt nucleation was found since the wettability contrast between the inner-square area and OTS grid was too low to confine droplets (both were too hydrophobic). These experimental results were consistent with our previous hypothesis that dewetting dynamics impacted

the CsX nucleation. We determined that MTS treatment with 6 min immersion was the ideal condition to obtain the CsX nucleus in a localized area for conversion into single crystal perovskite phase, for only one crystal per square area (Figure 2f). More quantitative analysis of the nucleation process can be found in SI2.

The as-prepared CsX samples were then converted into halide perovskite crystals *via* chemical vapor transportation (CVT). SEM images in Figure 2e and 2f show the perovskite (CsPbCl_3) formed from wetting substrate and partially wetting substrate, respectively. In both samples, every salt nucleus was converted into a cubic crystal. The chemical composition of the as-converted crystal was confirmed by photoluminescence (PL) mapping, which showed a strong emission wavelength at 423 nm (Figure 2e and 2f), and agrees with the reported emission wavelength of CsPbCl_3 ³. The wetting substrate resulted in multi-nuclei perovskite cubes with relatively small size and distributed randomly across the entire square area. On the contrary, partially wetting substrate mainly had one large CsPbCl_3 cube inside. It is worth mentioning that this conversion process began as a polycrystalline salt structure, and resulted in a single crystal perovskite. A melting-nucleation mechanism according to the phase diagram can explain this process. In this CVT process, PbX_2 (placed upstream) was continuously transported and reacted with CsX arrays (placed downstream), gradually changing the CsX: PbX_2 ratio. As shown on the CsBr-PbBr₂ phase diagram (see Figure S2), with

the amount of CsBr fixed, as the PbBr_2 ratio in the system gradually increased, the melting point of the CsBr and PbBr_2 mixture decreased. We hypothesize that the decreasing melting point could lead to a pre-melting process under our deposition temperature (400 degree Celsius). After the system passed the first eutectic point, the solid-phase CsPbBr_3 gradually precipitated from the solution, and slowly crystalized into single-crystalline perovskite structure, while the ratio between CsX and PbX_2 is 1:1. This process is further discussed in SI3.

A series of systematical characterization methods have been carried out to confirm the composition, morphology, and optical properties of as-synthesized perovskite arrays; CsPbCl_3 was also selected as a representative for discussion. Figure 3a shows an SEM image of CsPbCl_3 crystal arrays and the zoomed-in morphology in a square (Figure 3a inset). Each square is 10 μm by 10 μm with a distance of 10 μm apart from each other. From the SEM image, one can observe the contrast difference between the OTS layer (outside the square) and the inner-square area. The square areas in SEM images were marked by a white-dashed line. The chemical composition and distribution of corresponding elements in CsPbCl_3 plates were confirmed by energy-dispersive X-ray spectroscopy (EDS), showing that Cs, Pb and Cl were uniformly distributed in the crystal (Figure 3b), with the ratio of 1:0.96:2.63, which is roughly around 1:1:3 (See SI4, table 1). The PL spectrum was also used to confirm its composition (Figure 3c). The individual square plate

emitted at the wavelength of 423 nm, which agrees with reported emission of CsPbCl₃ crystals⁵. Figure 3c inset shows a confocal PL mapping of the individual plate with uniform emission, indicating a highly crystalline quality of the grown perovskite crystals. CsPbCl₃ crystal thickness was measured by atomic force microscopy (AFM), as shown in Figure 3 d-e, at a height of around 0.5 μm. The length and width of the crystal can also be measured *via* SEM, which is around 1.3 μm and 1.1 μm, respectively. Figure 3f shows a schematic of reconstructed CsPbCl₃ plate, which has comparable lengths in three dimensions. Furthermore, the size of CsPbCl₃ crystals was controlled by varying the size of the hydrophilic square area. By changing the length of the square area (2 μm, 5 μm, and 10 μm respectively), the CsPbCl₃ crystal width can be tuned from ~200 nm to 1.2 μm (Figure 3g inset from left to right). A linear relationship was observed between average length of the perovskites plate and length of the square area (Figure 3f); this indicates that the area of the square determines the volume of CsCl solution droplet confined, and further defines the final size of the perovskite crystal. Finally, large-area arrays were patterned with different sizes and geometries, and the PL panorama of all arrays are shown in Figure 3g. The PL emission from arrays also aligns with our confocal PL results, which further confirmed uniformity of the arrays.

Our two-step synthesis approach can also be generalized and extended to other halides. Figure 4 shows CsPbBr₃ and CsPbI₃ arrays that converted from

cesium bromide and cesium iodide, respectively. SEM images of the perovskite crystals arrays (left), a zoomed-in morphology (inset), and a corresponding PL image panorama (right) were shown in Figure 4a-b. An EDS mapping (Figure 4c) shows that all of the Cs, Pb and halide elements are uniformly distributed in the crystal, with a ratio roughly around 1:1:3 as well (more details shown in SI4, table 2-3). PL spectra of the array centered at 525 nm and 704 nm, respectively (Figure 4d), aligns with previous reports^{3, 38} and further confirms the chemical composition of the crystals. CsPbBr₃ arrays were converted with a slightly lower temperature compared to CsPbCl₃, due to the lower melting points of both CsBr and PbBr₂. It is also worth mentioning that due to structural differences between PbI₂ and the other two lead halides, the conversion strategy needs to be slightly modified. As a layered structure, PbI₂ crystals can easily nucleate into hexagonal flakes at lower energy nucleation sites. When the same method was used to grow CsPbI₃ arrays, instead of obtaining pure CsPbI₃ arrays, hexagonal PbI₂ flakes tended to form and grow from CsI, which served as a competing nucleation site (see Figure S4). Therefore, in this case, the growth approach needed to be slightly modified. CsI array was placed on top of the ceramics boat instead of being placed downstream. When PbI₂ precursors were heated to targeted temperature, the PbI₂ vapor directly reacted with CsI array and yielded highly crystalline, high-T phase CsPbI₃ plates. Furthermore, we scale up our patterning method to a 6-inch Si/SiO₂ wafer, as shown in Figure 4e. By dipping the pre-patterned wafer into CsX solution several times and taking it

out, CsX periodic arrays can be readily produced all at once. This demonstrates that our patterning method is robust and scalable, paving a way for industrial scale production for novel optoelectronic applications.

Conclusion

In conclusion, we have developed a two-step, bottom-up patterning method to grow single crystal metal halide perovskite arrays with tunable size and spacing in high yield. Polycrystalline CsX arrays are patterned on a hydrophilic/hydrophobic silicon substrate. Our work also provides scientific insight on the influence of surface wettability to crystal morphology during the dewetting process. The patterned CsX arrays are converted into single crystal perovskite arrays through a subsequent CVT process. Our method can be extended to different halides to realize all-inorganic metal halide perovskite arrays in three colors, and has the capability of state-of-arts scalable device fabrications, such as high spatial controllability and scalability. The ability to pattern all-inorganic perovskite arrays provides a platform for fundamental studies and for future novel optoelectronic applications.

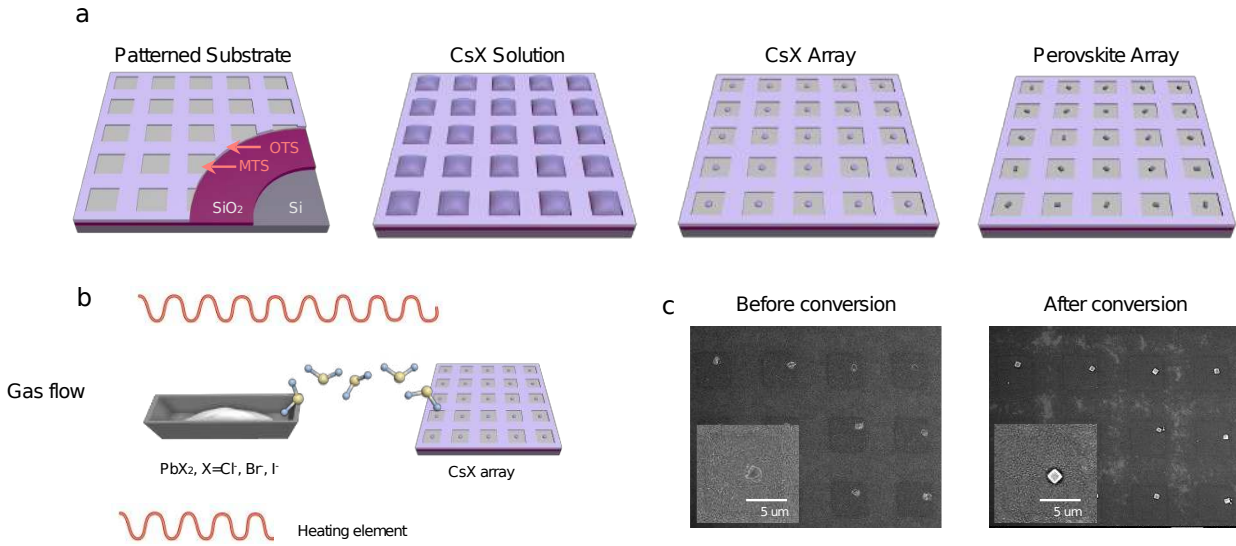


Figure 1. Schematic illustration, experimental setup and typical results of patterning process. (a) A schematic elucidating of the process from creating pre-patterned substrate, growth of CsX arrays and conversion of perovskite arrays. (b) A schematic showing the quartz tube and furnace heating element. The boat with PbX₂ is placed upstream and CsX arrays placed downstream. A nitrogen gas flow was maintained during the CVT process to transport PbX₂. (c) SEM image of as prepared salt arrays (left) and perovskite arrays after CVT conversion (right).

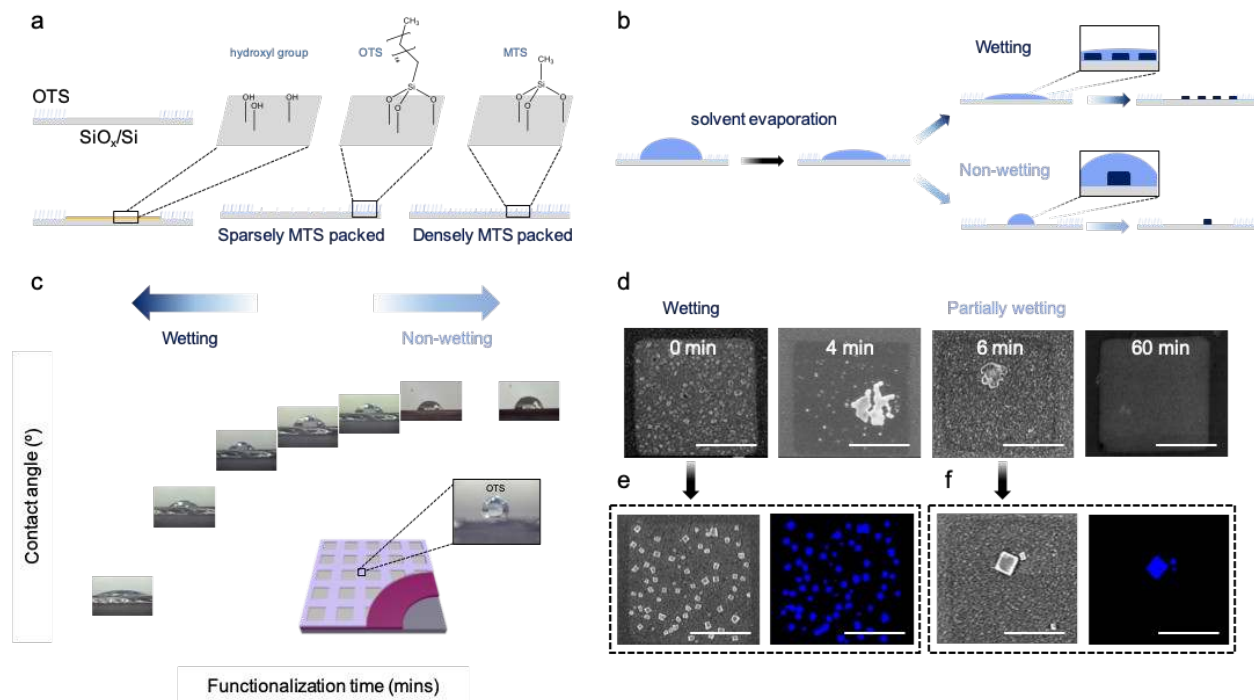


Figure 2. Schematics of patterning method and results. (a) Schematics of different surface conditions. Top row: surface with OH group, OTS and MTS respectively. Bottom row: Left: hydroxylation surface. Middle: sparsely MTS treated surface. Right: densely MTS treated surface. (b) Schematics elucidating interaction between droplet and surface in wetting (top row) and non-wetting (bottom row) case. (c) Contact angle changes with different MTS functionalization time. Inset: water droplet on OTS modified Si/SiO₂ substrate. (d) Morphology of CsCl with different MTS functionalization time. From left to right: 0 min, 4min, 6min and 60min. Scale bar: 5 μ m. (e-f) SEM and PL image of converted CsPbCl₃ on wetting (e) and partially wetting (f) substrates.

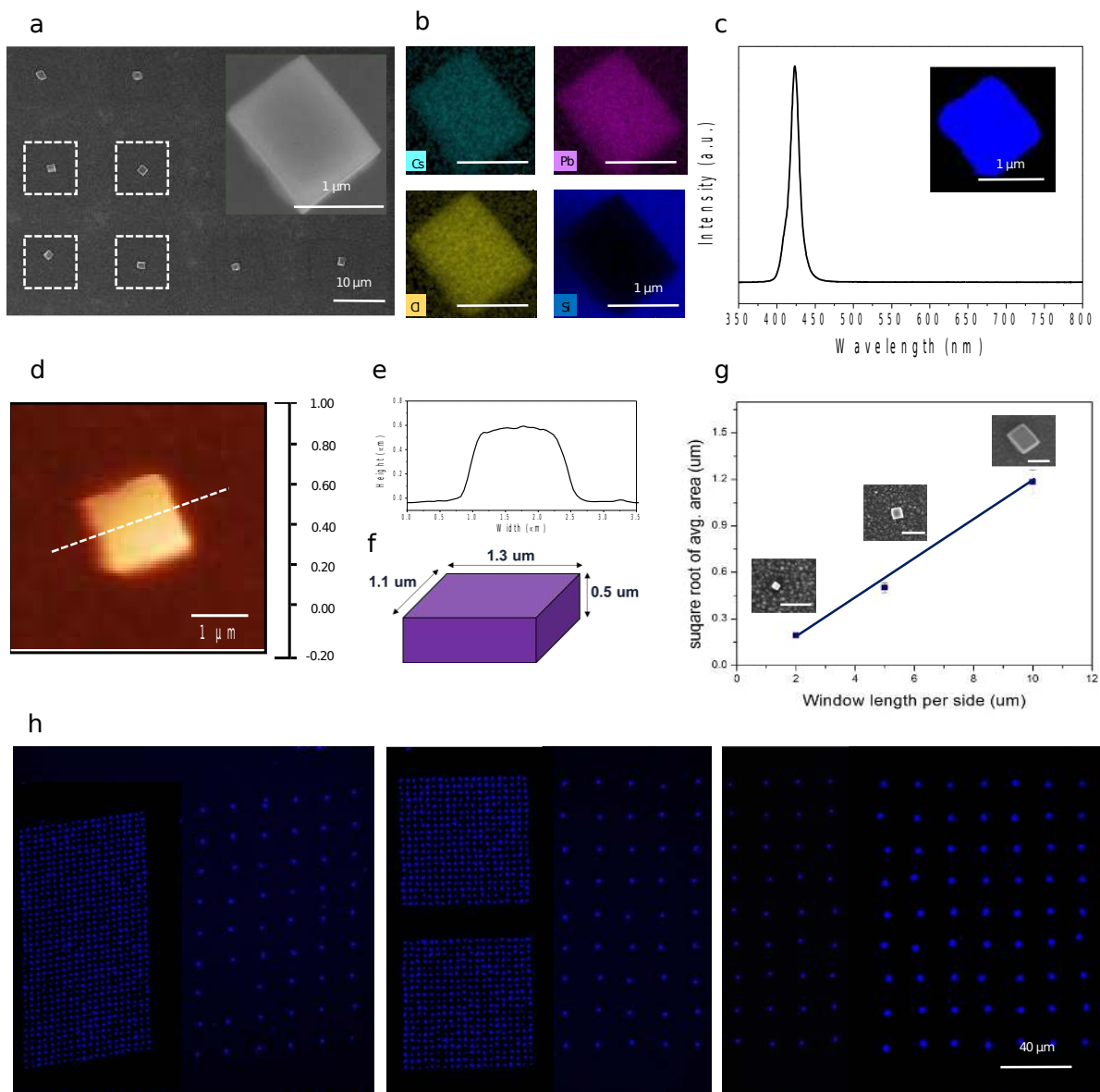


Figure 3. Characterizations of CsPbCl₃ arrays. (a) SEM images of as-grown perovskite arrays. Inset: zoomed-in SEM image of an individual plate. (b) SEM-EDS mapping of Cs, Pb, Cl and Si. (c) PL spectrum of the grown CsPbCl₃ array. Inset: PL image of an individual CsPbCl₃ plate. (d) AFM image and (e) height profile of a single CsPbCl₃ plate. (f) Schematic of reconstructed CsPbCl₃ plate. (g) Dependence of window length to square root of CsPbCl₃

area. Inset: SEM image of CsPbCl₃ with different sizes and geometry. (h) PL panorama of CsPbCl₃ arrays.

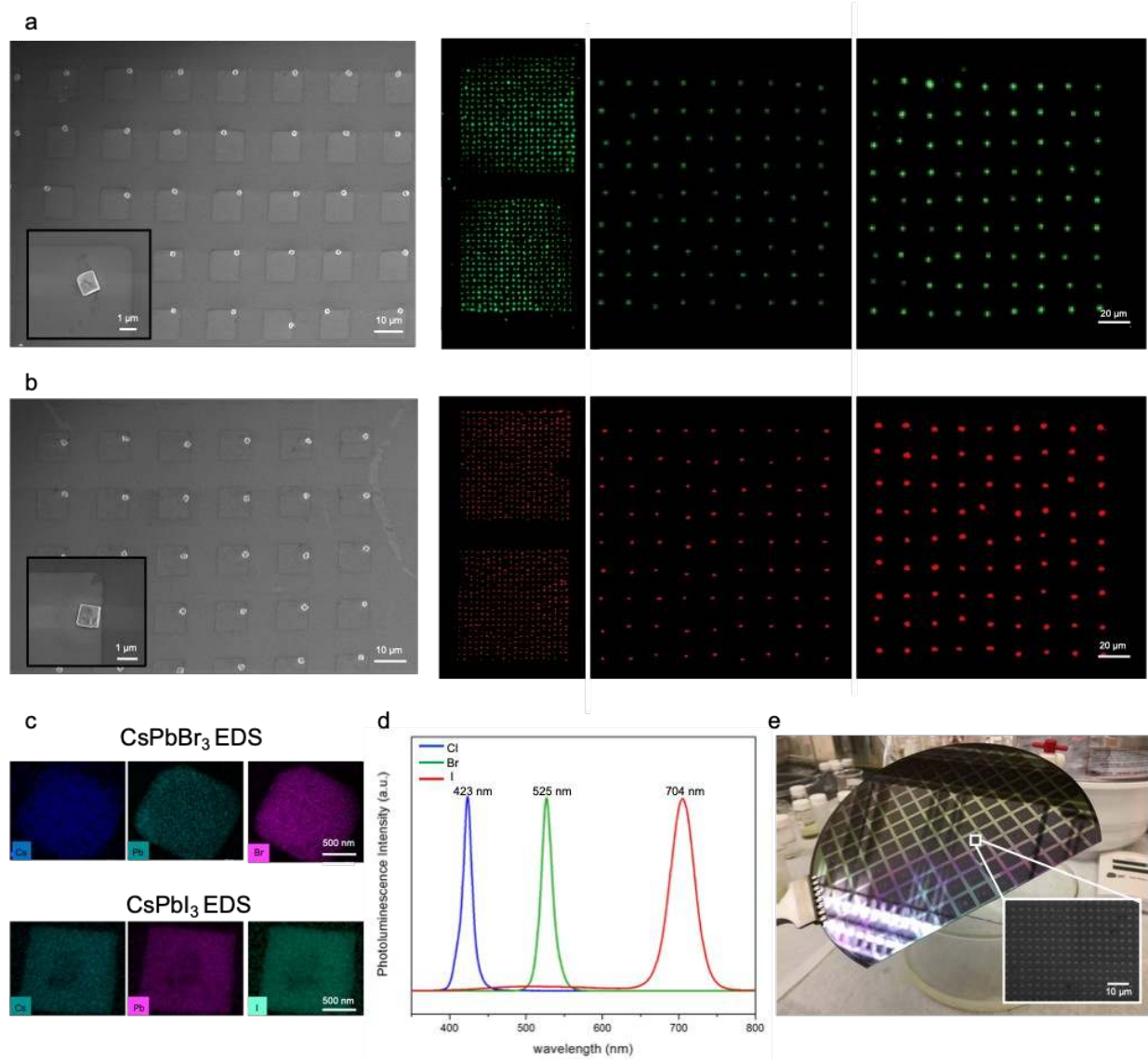


Figure 4. Characterizations of CsPbBr₃ and CsPbI₃ arrays. (a) Left: SEM image of CsPbBr₃ arrays. Scale bar: 10 μm. Inset: Zoomed-in image of a single CsPbBr₃ plate. Scale bar: 1 μm. Right: Panorama PL image of CsPbBr₃ arrays. Scale bar: 20 μm (b) Left: SEM image of CsPbI₃ array. Scale bar: 10 μm. Inset: Zoomed-in image of a single CsPbI₃ plate. Scale bar: 1 μm. Right: Panorama PL image of CsPbI₃ arrays.

Scale bar: 20 μm . (c) Top: SEM-EDS mapping of the CsPbBr_3 crystal. Bottom: SEM-EDS mapping of the CsPbI_3 crystal. Scale bar: 500 nm (d) PL spectrum of CsPbCl_3 (blue), CsPbBr_3 (green) and CsPbI_3 (red) respectively. (e) Photo of a 6-inch wafer. Entire wafer was dip-coated into CsCl solution and CsCl salt arrays can be created all at once.

AUTHOR INFORMATION

Corresponding Author

*Correspondence should be addressed to Peidong Yang
(p_yang@berkeley.edu)

Author Contributions

C.K.L., Q. Z., and P.Y. designed the experiments and wrote the paper. C.K. L. and Q.Z. grew and converted the CsPbX₃ array. C.K.L carried out optical spectroscopy measurements and confocal images. Q.Z. designed and performed the surface modification and contact angle measurements. Y.Z performed the AFM measurements. S.C. conducted the photolithography. C.K.L. and Q.K. performed SEM and EDX measurements. P.Y. supervised the project. All authors discussed the results and commented on the manuscript.

The authors declare no competing financial interest.

ACKNOWLEDGMENT

We thank Rachel Chan for helpful discussions on the work and manuscript preparation; Chris Jackson, Zhenni Lin and Mengyu Gao for fruitful discussion; This work was supported by the US Department of Energy, Office of Science, Office of Basic Energy Sciences, Materials Sciences and Engineering Division, under Contract DE-AC02-05CH11231 within the Physical Chemistry of Inorganic Nanostructures Program (KC3103). Confocal laser scanning microscopic study was conducted at the College of Natural Resources Biological Imaging Facility, supported in part by the National Institutes of Health S10 Program under Award 1S10RR026866-01. SEM-EDX performed at Molecular Foundry was supported by the Office of Science, Office of Basic Energy Science, of the U.S. Department of Energy. Y.Z., M.L., and Q.K. acknowledge the fellowship from Suzhou Industrial Park. S.C.-B. thanks the Philomathia Foundation for support. J.K. acknowledges IBS Global Postdoctoral Fellowship (IBS-R026-D1). C.K.L gratefully acknowledges Taiwan MOE scholarship.

References

- (1) Kim, Y.; Yassitepe, E.; Voznyy, O.; Comin, R.; Walters, G.; Gong, X.; Kanjanaboos, P.; Nogueira, A. F.; Sargent, E. H. Efficient Luminescence from Perovskite Quantum Dot Solids. *ACS Appl. Mater. Interfaces* **2015**, *7*, 25007-13.
- (2) Park, N.-G. Perovskite Solar Cells: An Emerging photovoltaic technology. *Mater. Today* **2015**, *18*, 65-72.
- (3) Protesescu, L.; Yakunin, S.; Bodnarchuk, M. I.; Krieg, F.; Caputo, R.; Hendon, C. H.; Yang, R. X.; Walsh, A.; Kovalenko, M. V. Nanocrystals of Cesium Lead Halide Perovskites (CsPbX_3 , X = Cl, Br, and I): Novel Optoelectronic Materials Showing Bright Emission with Wide Color Gamut. *Nano Lett.* **2015**, *15*, 3692-3696.
- (4) Xing, J.; Zhao, Y.; Askerka, M.; Quan, L. N.; Gong, X.; Zhao, W.; Zhao, J.; Tan, H.; Long, G.; Gao, L.; Yang, Z.; Voznyy, O.; Tang, J.; Lu, Z. H.; Xiong, Q.;

Sargent, E. H. Color-stable Highly Luminescent Sky-blue Perovskite Light-emitting Diodes. *Nat. Commun.* **2018**, 9, 3541.

(5) Wang, H.; Kim, D. H. Perovskite-based Photodetectors: Materials and Devices. *Chem. Soc. Rev.* **2017**, 46, 5204-5236.

(6) Tsai, W.-L.; Chen, C.-Y.; Wen, Y.-T.; Yang, L.; Cheng, Y.-L.; Lin, H.-W. Band Tunable Microcavity Perovskite Artificial Human Photoreceptors. *Adv. Mater.* **2019**, 31, 1900231.

(7) Wu, J.; Chen, J.; Zhang, Y.; Xu, Z.; Zhao, L.; Liu, T.; Luo, D.; Yang, W.; Chen, K.; Hu, Q.; Ye, F.; Wu, P.; Zhu, R.; Gong, Q. Pinhole-Free Hybrid Perovskite Film with Arbitrarily-Shaped Micro-Patterns for Functional Optoelectronic Devices. *Nano Lett.* **2017**, 17, 3563-3569.

(8) Choi, C.; Choi, M. K.; Liu, S.; Kim, M. S.; Park, O. K.; Im, C.; Kim, J.; Qin, X.; Lee, G. J.; Cho, K. W.; Kim, M.; Joh, E.; Lee, J.; Son, D.; Kwon, S.-H.; Jeon, N. L.; Song, Y. M.; Lu, N.; Kim, D.-H. Human Eye-inspired Soft Optoelectronic Device Using High-density MoS₂-graphene Curved Image Sensor Array. *Nat. Commun.* **2017**, 8, 1664.

(9) Wang, Y.-C.; Li, H.; Hong, Y.-H.; Hong, K.-B.; Chen, F.-C.; Hsu, C.-H.; Lee, R.-K.; Conti, C.; Kao, T. S.; Lu, T.-C. Flexible Organometal-Halide Perovskite Lasers for Speckle Reduction in Imaging Projection. *ACS Nano* **2019**, 13, 5421-5429.

(10) Eaton, S. W.; Lai, M.; Gibson, N. A.; Wong, A. B.; Dou, L.; Ma, J.; Wang, L.-W.; Leone, S. R.; Yang, P. Lasing in Robust Cesium Lead Halide Perovskite Nanowires. *P. Natl. Acad. Sci. USA* **2016**, 113, 1993.

- (11) Misra, R. K.; Aharon, S.; Li, B.; Mogilyansky, D.; Visoly-Fisher, I.; Etgar, L.; Katz, E. A. Temperature- and Component-Dependent Degradation of Perovskite Photovoltaic Materials under Concentrated Sunlight. *J Phys. Chem. Lett.* **2015**, 6, 326-330.
- (12) Berhe, T. A.; Su, W.-N.; Chen, C.-H.; Pan, C.-J.; Cheng, J.-H.; Chen, H.-M.; Tsai, M.-C.; Chen, L.-Y.; Dubale, A. A.; Hwang, B.-J. Organometal Halide Perovskite Solar Cells: Degradation and Stability. *Energ. Environ. Sci.* **2016**, 9, 323-356.
- (13) Yang, X.; Wu, J.; Liu, T.; Zhu, R. Patterned Perovskites for Optoelectronic Applications. *Small Methods* **2018**, 2, 1800110.
- (14) Gu, Z.; Wang, K.; Li, H.; Gao, M.; Li, L.; Kuang, M.; Zhao, Y. S.; Li, M.; Song, Y. Direct-Writing Multifunctional Perovskite Single Crystal Arrays by Inkjet Printing. *Small* **2017**, 13, 1603217.
- (15) Zhou, N.; Bekenstein, Y.; Eisler, C. N.; Zhang, D.; Schwartzberg, A. M.; Yang, P.; Alivisatos, A. P.; Lewis, J. A. Perovskite nanowire-block copolymer composites with digitally programmable polarization anisotropy. *Sci. Adv.* **2019**, 5, eaav8141.
- (16) Liu, Y.; Li, F.; Qiu, L.; Yang, K.; Li, Q.; Zheng, X.; Hu, H.; Guo, T.; Wu, C.; Kim, T. W. Fluorescent Microarrays of in Situ Crystallized Perovskite Nanocomposites Fabricated for Patterned Applications by Using Inkjet Printing. *ACS Nano* **2019**, 13, 2042-2049.

- (17) Zhao, C.; Li, H.; Wang, Y.; Li, K.; Hou, J.; Ma, Y.; Li, M.; Song, Y. A General Layer-by-Layer Printing Method for Scalable High-Resolution Full-Color Flexible Luminescent Patterns. *Adv. Optical Mat.* **2019**, *7*, 1900127.
- (18) Zhu, M.; Duan, Y.; Liu, N.; Li, H.; Li, J.; Du, P.; Tan, Z.; Niu, G.; Gao, L.; Huang, Y.; Yin, Z.; Tang, J. Electrohydrodynamically Printed High-Resolution Full-Color Hybrid Perovskites. *Adv. Funct. Mater.* **2019**, *29*, 1903294.
- (19) Wong, Y. C.; Wu, W. B.; Wang, T.; Ng, J. A.; Khoo, K. H.; Wu, J.; Tan, Z. K. Color Patterning of Luminescent Perovskites via Light-Mediated Halide Exchange with Haloalkanes. *Adv. Mater.* **2019**, e1901247.
- (20) Alias, M. S.; Dursun, I.; Shi, D.; Saidaminov, M. I.; Diallo, E. M.; Priante, D.; Ng, T. K.; Bakr, O. M.; Ooi, B. S. Focused-ion Beam Patterning of Organolead Trihalide Perovskite for Subwavelength Grating Nanophotonic Applications. *J. Vac. Sci. Technol. B* **2015**, *33*, 051207.
- (21) Chou, S. S.; Swartzentruber, B. S.; Janish, M. T.; Meyer, K. C.; Biedermann, L. B.; Okur, S.; Burckel, D. B.; Carter, C. B.; Kaehr, B. Laser Direct Write Synthesis of Lead Halide Perovskites. *J Phys. Chem. Lett.* **2016**, *7*, 3736-3741.
- (22) Alias, M. S.; Yang, Y.; Ng, T. K.; Dursun, I.; Shi, D.; Saidaminov, M. I.; Priante, D.; Bakr, O. M.; Ooi, B. S. Enhanced Etching, Surface Damage Recovery, and Submicron Patterning of Hybrid Perovskites using a Chemically Gas-Assisted Focused-Ion Beam for Subwavelength Grating Photonic Applications. *J Phys. Chem. Lett.* **2016**, *7*, 137-42.

(23) Wang, H.; Haroldson, R.; Balachandran, B.; Zakhidov, A.; Sohal, S.; Chan, J. Y.; Zakhidov, A.; Hu, W. Nanoimprinted Perovskite Nanograting Photodetector with Improved Efficiency. *ACS Nano* **2016**, *10*, 10921-10928.

(24) Jeong, B.; Hwang, I.; Cho, S. H.; Kim, E. H.; Cha, S.; Lee, J.; Kang, H. S.; Cho, S. M.; Choi, H.; Park, C. Solvent-Assisted Gel Printing for Micropatterning Thin Organic-Inorganic Hybrid Perovskite Films. *ACS Nano* **2016**, *10*, 9026-9035.

(25) Kim, W.; Jung, M. S.; Lee, S.; Choi, Y. J.; Kim, J. K.; Chai, S. U.; Kim, W.; Choi, D.-G.; Ahn, H.; Cho, J. H.; Choi, D.; Shin, H.; Kim, D.; Park, J. H. Oriented Grains with Preferred Low-Angle Grain Boundaries in Halide Perovskite Films by Pressure-Induced Crystallization. *Adv. Energy Mat.* **2018**, *8*, 1702369.

(26) Niu, L.; Liu, X.; Cong, C.; Wu, C.; Wu, D.; Chang, T. R.; Wang, H.; Zeng, Q.; Zhou, J.; Wang, X.; Fu, W.; Yu, P.; Fu, Q.; Najmaei, S.; Zhang, Z.; Yakobson, B. I.; Tay, B. K.; Zhou, W.; Jeng, H. T.; Lin, H.; Sum, T. C.; Jin, C.; He, H.; Yu, T.; Liu, Z. Controlled Synthesis of Organic/Inorganic van der Waals Solid for Tunable Light-Matter Interactions. *Adv. Mater.* **2015**, *27*, 7800-7808.

(27) Wu, C. Y.; Wang, Z.; Liang, L.; Gui, T.; Zhong, W.; Du, R. C.; Xie, C.; Wang, L.; Luo, L. B. Graphene-Assisted Growth of Patterned Perovskite Films for Sensitive Light Detector and Optical Image Sensor Application. *Small* **2019**, *15*, e1900730.

(28) Wang, G.; Li, D.; Cheng, H.-C.; Li, Y.; Chen, C.-Y.; Yin, A.; Zhao, Z.; Lin, Z.; Wu, H.; He, Q. Wafer-scale growth of large arrays of perovskite microplate

crystals for functional electronics and optoelectronics. *Sci. Adv.* **2015**, 1, e1500613.

(29) Huang, J.; Lai, M.; Lin, J.; Yang, P. Rich Chemistry in Inorganic Halide Perovskite Nanostructures. *Adv. Mater.* **2018**, 30, e1802856.

(30) Saliba, M.; Matsui, T.; Domanski, K.; Seo, J.-Y.; Ummadisingu, A.; Zakeeruddin, S. M.; Correa-Baena, J.-P.; Tress, W. R.; Abate, A.; Hagfeldt, A.; Grätzel, M. Incorporation of Rubidium Cations into Perovskite Solar Cells Improves Photovoltaic Performance. *Science* **2016**, 354, 206-209.

(31) McMeekin, D. P.; Sadoughi, G.; Rehman, W.; Eperon, G. E.; Saliba, M.; Hörantner, M. T.; Haghighirad, A.; Sakai, N.; Korte, L.; Rech, B.; Johnston, M. B.; Herz, L. M.; Snaith, H. J. A Mixed-cation Lead Mixed-halide Perovskite Absorber for Tandem Solar Cells. *Science* **2016**, 351, 151-155.

(32) Qin, D.; Xia, Y.; Xu, B.; Yang, H.; Zhu, C.; Whitesides, G. M. J. A. M. Fabrication of Ordered Two-Dimensional Arrays of Micro- and Nanoparticles Using Patterned Self-Assembled Monolayers as Templates. *Adv. Mater.* **1999**, 11, 1433-1437.

(33) Rio, E.; Daerr, A.; Lequeux, F.; Limat, L. Moving Contact Lines of a Colloidal Suspension in the Presence of Drying. *Langmuir.* **2006**, 22, 3186-3191.

(34) Cheng, W.; Park, N.; Walter, M. T.; Hartman, M. R.; Luo, D. Nanopatterning Self-Assembled Nanoparticle Superlattices by Moulding Microdroplets. *Nat. Nanotechnol.* **2008**, 3, 682-90.

(35) Orejon, D.; Sefiane, K.; Shanahan, M. E. Stick-Slip of Evaporating Droplets: Substrate Hydrophobicity and Nanoparticle Concentration. *Langmuir*. **2011**, 27, 12834-43.

(36) Bourges-Monnier, C.; Shanahan, M. J. L. Influence of Evaporation on Contact Angle. *Langmuir*. **1995**, 11, 2820-2829.

(37) McHale, G.; Rowan, S. M.; Newton, M. I.; Banerjee, M. K. Evaporation and the Wetting of a Low-Energy Solid Surface. *J. Phys. Chem. B* **1998**, 102, 1964-1967.

(38) Lai, M.; Kong, Q.; Bischak, C. G.; Yu, Y.; Dou, L.; Eaton, S. W.; Ginsberg, N. S.; Yang, P. Structural, Optical, and Electrical Properties of Phase-controlled Cesium Lead Iodide Nanowires. *Nano Research* **2017**, 10, 1107-1114.